Journal of Power Sources 195 (2010) 2248–2259

Contents lists available at ScienceDirect

Journal of Power Sources

journal homepage: www.elsevier.com/locate/jpowsour

Analysis of heat and mass transport in a miniature passive and semi passive liquid-feed direct methanol fuel cell

Bin Xiao, Hafez Bahrami, Amir Faghri*

Department of Mechanical Engineering, University of Connecticut, 261 Glenbrook Road, Unit 2337, Storrs, CT 06169, United States

ARTICLE INFO

Article history:
Received 31 August 2009
Received in revised form 15 October 2009
Accepted 16 October 2009
Available online 27 October 2009

Keywords:
Fuel cell
Passive and semi passive DMFC
Two-phase heat and mass transport
Thermal management

ABSTRACT

A two-dimensional, transient, multi-phase, multi-component, and non-isothermal model has been developed to solve the heat and mass transport in a passive and semi passive liquid-feed direct methanol fuel cell (DMFC). A semi passive DMFC uses channel at the cathode side to facilitate the oxidant transport. The transient characteristics of the temperature, methanol concentration, methanol crossover, useful current density and methanol evaporation are investigated. The results indicate that the temperature in the fuel cell increases during operation as much as 10 °C, due to the heat generation by internal phase change and the electrochemical reactions. However, it is revealed that the temperature distribution is nearly uniform at any time through all porous layers including the fuel cell and fuel delivery system. The effect of using an active feeding system in the cathode and passive methanol feeding in the anode (semi passive system) on the performance of a fuel cell is also studied. The active oxidant feeding to the cathode catalyst layer in the semi passive cell improved the fuel cell performance compared to that in a passive one. However, in general, the performance of passive cell is better than that in a semi passive one because of more temperature increase in the passive system.

Published by Elsevier B.V.

1. Introduction

The direct methanol fuel cell (DMFC) has gained much attention in recent years as a promising portable power source because of its advantages over traditional electrical energy including long durability, ease of storage and transport, simple structure, and low cost [1–3]. However, the industrial application of a DMFC is still hindered by several technical challenges such as low electrochemical activity at the anode due to intermediate reactants and species during methanol oxidation, mixed potential at the cathode due to the direct methanol oxidation by the methanol crossover through the membrane, and the performance deterioration caused by the generated water flooding the cathode [4,5].

In a conventional DMFC, "active" delivery techniques are applied to feed the reactants into the fuel cell with a pump or fan [6,7]. In order to minimize the parasitic power losses due to using a pump or fan and decrease the volume and the weight, passive-feed approaches without external moving parts have been applied in DMFC design. In the passive DMFCs, the oxygen diffuses into the cathode catalyst layer from the ambient air by an air breathing action, and the methanol diffuses into the anode from the feed reservoir driven by various internal forces such as concentration gradient and capillary forces in the wick structures.

Experimental investigations on the various DMFC systems that operate under passive conditions have been done to analyze the parametric effects and improve the power density or energy conversion efficiency [8–11]. Guo and Faghri [8,9] developed an innovative passive fuel delivery DMFC that can deliver pure methanol from the reservoir to the fuel cell by using preferential and non-preferential porous media between the reservoir and the fuel cell. They developed a new liquid-feed miniature passive DMFC system that includes a fuel cell stack, a fuel tank, and a passive ancillary system. With 5.1 g of neat methanol in the fuel cartridge, a prototype has successfully demonstrated 18 h of continuous operation with total power output of 1.56 W h. Their system can be used in a window-frame planner stack configuration; therefore the total desirable cell output power is easily adjustable [9].

The DMFC performance developments not only rely on the material development such as better catalysts or polymer electrolyte membranes with less permeability for methanol and water, but also the optimal design related to the operation conditions, physical and electrochemical parameters, and geometric design parameters including the passive ancillary systems [12–17]. These parameters are coupled in the complex physicochemical processes, including the heat/mass transport and multiple electrochemical reactions. Since it is hard to quantify the complex processes inside a DMFC directly by experiments, the mathematical modeling can

* Corresponding author. Tel.: +1 860 486 0419.
E-mail address: amir.faghri@uconn.edu (A. Faghri).

0378-7753/$ – see front matter. Published by Elsevier B.V.
doi:10.1016/j.jpowsour.2009.10.047

Nomenclature

a	longer edge of rectangular duct (m)
a_{ox}	specific area for oxidation (m^{-1})
a_{red}	specific area for reduction (m^{-1})
b	shorter edge of rectangular duct (m)
$\mathbf{B}$	coefficient matrix for Stefan–Maxwell ($s\,m^{-2}$)
C_{MeOH}	liquid methanol concentration ($mol\,cm^{-3}$)
C_{H_2O}	liquid water concentration ($mol\,cm^{-3}$)
D_{ij}	binary diffusivity ($m^2\,s^{-1}$)
$D_{eff,ij}$	effective diffusivity of gas phase ($m^2\,s^{-1}$)
F	Faraday constant ($Coulomb\,mol^{-1}$)
Gr	Grashof number
g	gravity ($m\,s^{-2}$)
h	heat transfer coefficient ($W\,m^{-1}\,K^{-1}$)
h_{fg}	latent heat of vaporization ($J\,kg^{-1}$)
h_{m1}	mass transfer coefficient on the air breathing surface ($kg\,m^{-2}\,s^{-1}$)
$I_{0,ref}^{MeOH}$	oxidation exchange current density ($A\,m^{-2}$)
$I_{0,ref}^{O_2}$	reduction exchange current density ($A\,m^{-2}$)
I	current density ($A\,m^{-2}$)
$I_{crossover}$	crossover current density ($A\,m^{-2}$)
$J(s)$	Leverette function
k_{rg}	relative permeability of gas phase
k_{rl}	relative permeability of liquid phase
k	permeability (m^2)
L	characteristic length (m)
Le	Lewis number
$\dot{m}'''$	mass source ($kg\,m^{-3}\,s^{-1}$)
M_i	molecular weight of component i ($kg\,mol^{-1}$)
M_g	molecular weight of gas ($kg\,mol^{-1}$)
M_l	molecular weight of liquid ($kg\,mol^{-1}$)
NPW	none preferential Wick
n	normal vector to the surface
n_d	electro osmotic drag coefficient for pure water ($mol\,mol^{-1}$)
Nu	Nusselt number
PW	preferential wick
Pr	Prandtl number
p_c	capillary pressure (Pa)
p_l	liquid pressure (Pa)
p_g	gas pressure (Pa)
R_u	universal gas constant ($J\,mol^{-1}\,K^{-1}$)
R_{ox}	oxidation reaction rate ($A\,m^{-3}$)
R_{red}	reduction reaction rate ($A\,m^{-3}$)
s	liquid saturation
S	source terms
Sc	Schmidt number
Sh	Sherwood number
t	time (s)
T	temperature (K)
V	volume (m^3)
V_k	velocity of phase k ($m\,s^{-1}$)
$\langle V_k \rangle^k$	intrinsic phase velocity of phase k ($m\,s^{-1}$)
x_{MeOH}	mole fraction of liquid methanol ($mol\,mol^{-1}$)
x	distance in x-direction (m)
y	distance in y-direction (m)

Greek symbols

α_l	liquid volume fraction
$\alpha_{l,MeOH}$	volume fraction of MeOH in liquid phase
α_a	anode transfer coefficient
α_c	cathode transfer coefficient
ε	porosity
ϕ	potential (V)
η	fuel consumption efficiency
η_a	anode over potential (V)
η_c	cathode over potential (V)
λ	oxidation constant ($mol\,cm^{-3}$)
μ	viscosity ($N\,s\,m^{-2}$)
θ	contact angle between liquid and solid (radians)
σ	surface tension ($N\,m^{-1}$)
σ_c	electrical conductivity of carbon phase ($\Omega^{-1}\,m^{-1}$)
σ_m	proton conductivity in membrane phase ($\Omega^{-1}\,m^{-1}$)
ρ	density ($kg\,m^{-3}$)
τ	tortuosity
$\omega_{g,i}$	mass fraction of ith gas species ($kg\,kg^{-1}$)
$\omega_{l,i}$	mass fraction of ith liquid species ($kg\,kg^{-1}$)

Subscripts

acl	anode catalyst layer
agdl	anode gas diffusion layer
c	carbon cloth
ccl	cathode catalyst layer
cgdl	cathode gas diffusion layer
dar	Darcy
ele	electro osmotic drag
g	gas
gl	gas to liquid
i	component i
ini	initial
j	component j
l	liquid
m	membrane
max	maximum
pc	phase change
r	due to chemical reaction
ref	Reference value
T	due to mass transport (evaporation/condensation)
Ω	Ohmic heating

act as an effective design tool to investigate the physicochemical phenomena and performance characteristic of the DMFCs.

Numerous models for active and passive DMFCs were found in the literature ranging in the dimensional and the physical characteristic that they capture [18–43]. Table 1 summarizes the major features of the most recent publications in the numerical modeling of DMFC. In this table, the first five columns are devoted to the investigators, dimension of the model, steady or unsteady modeling, capturing the thermal effect, and single- or two-phase flow modeling, respectively. The sixth column shows the two-phase modeling approach which can be multi-fluid, mixture, or unsaturated flow theory. Since a DMFC is a multi-component system in both gaseous and liquid phases, it is important to capture the mutual effect of the species in the diffusion through the porous media. To capture this effect, Stefan–Maxwell model should be used instead of Fick's law which is appropriate for a binary mixture. This is described in column seven. Column eight describes the type of approximation for the momentum equation at the porous layers of a DMFC. The local chemical equilibrium and non-equilibrium condition at the interface between gas and liquid phases at the porous layers are given in the ninth column. All the modeling based on the mixture approach can only capture the local chemical equilibrium condition at the interface. It implies that for a condensable species at the interface between liquid and gas phases in an instantaneous time the mass flux from liquid to gas equals the mass flux

Table 1
Summary of the features of the recent publications in the numerical modeling of DMFC.

Investigator	1D/2D/3D	Steady/ unsteady	Isothermal/ non-isothermal	Single/ two-phase modeling	Two-phase flow modeling approach	Mass diffusion model for gas phase	Darcy/ Brinkman's/full N.S.	Chemical equilibrium/non-equilibrium	Single/ multi-domain	Solving electro-chemical potential	Air supply	Fuel supply (MeOH)	Water diffusion through the membrane
2000-Kolikovsky [18]	2D	St.[a]	Iso.[b]	Single ph.	N/A[c]	Stef.–Max[d]	Darcy	N/A	Multi	Yes	Air (active)	Liquid (active)	No
2002-Meyers and Newman [19–21]	N/A	St.	Iso.	Two ph.	Multi-fluid	Stef.–Max	N/A	Equib.	Multi	Yes	N/A	N/A	Yes
2003-Divisek et al. [22]	2D	Unst.	Non-Iso.	Two ph.	Multi-fluid	Stef.–Max	Darcy	Non. Eq.	Single	Yes	Air (active)	Liquid (active)	No
2003-Wang and Wang [23]	2D	Unst.	Iso.	Two ph.	Mixture	Fick's law	Darcy	Equib.	Multi	No	Air (active)	Liquid (active)	No
2004-Birgersson et al. [24]	2D	St.	Iso.	Two ph.	Mixture	Fick's law	Darcy	Equib.	Single	No	Anode modeling	Liquid (active)	No
2006-Ge and Liu [25]	3D	St.	Iso.	Two ph.	N/A	Fick's law	Full N.S.	N/A	Multi	No	Air channel (active)	Liquid (active)	N/A
2006-Ge and Liu [26]	3D	St.	Iso.	Two ph.	Mixture	Fick's law	Full N.S.	Equib.	Multi	No	Air channel (active)	Liquid (passive)	N/A
2007-Rice and Faghri [27]	2D	Unst.	Iso.	Two ph.	Multi-fluid	Stef.–Max	Darcy	Non. Eq.	Single	Yes	Air breathing	Liquid (passive)	No
2007-Liu and Wang [28]	3D	Unst.	Iso.	Two ph.	Mixture	Fick's law	Full N.S.[e]	Equib.	Multi	Yes	Air (active)	Liquid (active)	Yes
2007-Saarinen et al. [29]	3D	St.	Iso.	Single ph.	N/A	Stef.–Max	Brinkman	N/A	Multi	No	Air (active)	Liquid (active)	No
2007-Yang and Zhao [30]	2D	St.	Iso.	Two ph.	Multi-fluid	Fick's law	Darcy	Non. Eq.	Multi	No	Air (active)	Liquid (active)	No
2007-Liu and Wang [31]	3D	Unst.	Iso	Two ph.	Mixture	Fick's law	Full N.S.	Equib.	Multi	Yes	Air (active)	Liquid (active)	Yes
2007-Yang et al. [32]	3D	St.	Iso.	Two ph.	Multi-fluid	Fick's law	Darcy	Non. Eq.	Multi	No	Air (active)	Liquid (active)	No
2007-Yang and Zhao [33]	2D	St.	Iso.	Two ph.	Multi-fluid	Fick's law	Darcy	Non. Eq.	Multi	No	Air (active)	Liquid (active)	No
2007-Yan and Jen [36]	2D	St.	Iso.	Two ph.	Mixture	Fick's law	Full N.S.	Equib.	Single	No	Air channel (active)	Liquid (active)	No
2008-Xu et al. [34]	1D	St.	Iso.	Two ph.	Multi-fluid	Fick's law	Darcy	Non. Eq.	Multi	No	Air breathing	Liquid (passive)	Yes
2008-Chen et al. [35]	2D	St.	Non-Iso.	Two ph.	Unsaturated flow theory	Fick's law	Darcy	Non. Eq.	Multi	No	Air breathing	Liquid (passive)	No
2008-Xiao and Faghri [37]	2D	Unst.	Non-Iso.	Two ph.	Multi-fluid	Stef.–Max	Darcy	Equib.	Single	Yes	Air breathing	Liquid (passive)	No
2008-Rice and Faghri [38]	1D	Unst.	Non-Iso.	Two ph.	Multi-fluid	Stef.–Max	Darcy	Equib.	Single	Yes	Air breathing	Vapor. (passive)	No
2008-Rice and Faghri [39]	2D	Unst.	Non-Iso.	Two ph.	Multi-fluid	Stef.–Max	Darcy	Equib.	Single	Yes	Air breathing	Liquid (passive)	No
2008-Yang and Zhao [40]	2D	Unst.	Iso.	Two ph.	Multi-fluid	Fick's law	Darcy	Non. Eq.	Multi	No	Air (active)	Liquid (passive)	No
2009-Xiao and Faghri [41]	2D	Unst.	Non-Iso.	Two ph.	Multi-fluid	Stef.–Max	Darcy	Equib.	Single	Yes	Air breathing	Liquid (passive)	No
2009-Jewett et al. [42]	2D	Unst.	Non-Iso.	Two ph.	Multi-fluid	Stef.–Max	Darcy	Equib.	Single	Yes	Air breathing	Liquid (passive)	No
Birgersson, E., et al. [24]	2D	St.	Iso.	Two ph.	Mixture	Fick's law	Darcy	Equib.	Single	No	Anode modeling	Liquid (active)	No

[a] St./Unst. refers to steady and unsteady.
[b] Iso. refers to isothermal.
[c] N/A refers to not applicable.
[d] Stef.–Max refers to Stefan–Maxwell equation.
[e] N.S. refers to Navier–Stokes equation.

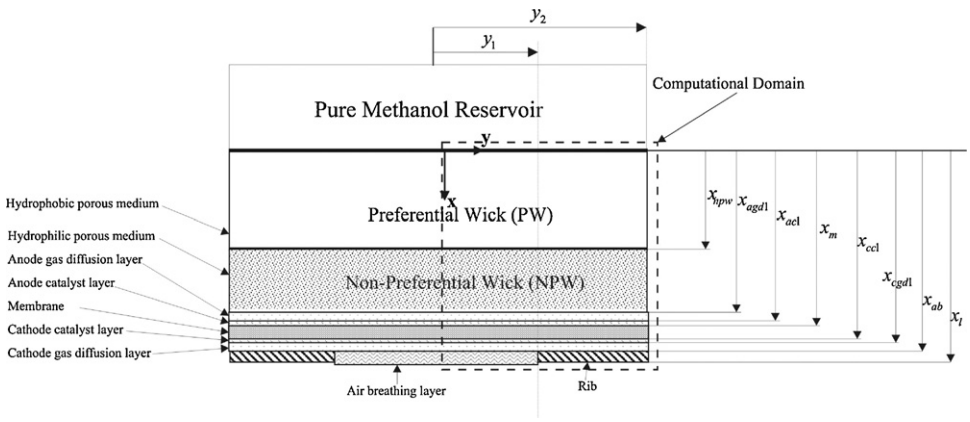

Fig. 1. Schematic diagram of a passive liquid-feed DMFC.

from gas to liquid phase. Since DMFCs are composed of many different porous layers, the numerical model can consider all layers as a single domain with appropriate boundary conditions at the outer boundary, or it can deal with layers separately with multiple inner boundary conditions (multi-domain simulation). These two approaches are given in the tenth column. The last four columns describe whether the model considers the electrochemical potential or not, air supplying system to the cathode side, fuel supplying at the anode, and the liquid saturation value at the cathode gas diffusion layer, respectively.

A review of literatures shows that even though there are some investigators [24,26,30] who have made a comparison between single-phase and two-phase modeling of a DMFC, and also between chemical equilibrium and non-equilibrium approaches, none of the previous non-isothermal models in the liquid-feed DMFC [22,35,37,39] focused on the effect of the temperature increase on the characteristic phenomena. In this study, a 2D, non-isothermal, transient model based on the multi-fluid approach is developed to capture the advantage of a non-isothermal model over an isothermal one for a passive DMFC system. Furthermore, motivated by achieving higher output power density, the performance of a semi passive DMFC and the effect of using a passive fuel delivery system at the anode and supplying the oxidant at the cathode by using forced convection are investigated. To study the effect of each parameter independently, first the effect of temperature on the semi passive cell performance is investigated, and at the next step the effect of using a forced mass transport on the performance of an isothermal semi passive cell is studied.

2. Physical model

The schematic of a passive DMFC delivery system and the membrane exchange assembly is illustrated in Fig. 1. The system can be divided into three parts: (1) a methanol delivery part including a reservoir filled with pure methanol, preferential wicking (PW) material to prevent back diffusion of water into the reservoir, and the non-preferential wick (NPW) material to deliver the methanol to the fuel cell and control the methanol concentration at the anode side; (2) a fuel cell which includes anode and cathode gas diffusion layers, catalyst layers and a polymer electrolyte membrane; (3) an air breathing part made of hydrophobic materials to prevent water droplet formation on the cathode side. The following assumptions are used in the model:

- The MeOH concentration in the reservoir remains constant during fuel cell operation.

Table 2
Governing equations for a passive liquid-feed DMFC system.

Conservation equation	General form of equation	
Liquid phase		
Mass	$\frac{D}{Dt}(\varepsilon s\rho_l) = S_{\dot{m}_l}$	(1)
Momentum [44]	$\frac{D}{Dt}(\varepsilon s\rho_l \langle V_l \rangle^{\ell}) = -\nabla P_l + \nabla(\mu_l \nabla \langle V_l \rangle^{\ell}) + \rho_l g + S_{l,dar} + S_{l,ele}$	(2)
Species	$\frac{D}{Dt}(\varepsilon s\rho_l \omega_{l,i}) = \nabla([\varepsilon s]^{\tau}\rho_l D_{l,12}\nabla\omega_{l,i}) + \dot{m}'''_{l,r,i} + \dot{m}'''_{T,gl,i}$	(3)
Gas phase		
Mass	$\frac{D}{Dt}(\varepsilon(1-s)\rho_g) = S_{\dot{m}_g}$	(4)
Momentum [44]	$\frac{D}{Dt}(\varepsilon(1-s)\rho_g \langle V_g \rangle^{g}) = -\nabla(P_g) + \nabla\left(\mu_g \nabla \langle V_g \rangle^{g}\right) + \rho_g g + S_{g,dar}$	(5)
Species	$\frac{D}{Dt}(\varepsilon(1-s)\rho_g \omega_{g,i}) = \nabla([\varepsilon(1-s)]^{\tau}\rho_g D_{eff,ij}\nabla\omega_{g,i}) + \dot{m}'''_{g,r,i} - \dot{m}'''_{T,gl,i}$	(6)
Thermal energy [39]	$\frac{D}{Dt}\sum(\varepsilon s\rho_{l,i}c_{p,l,i}T + \varepsilon(1-s)\rho_{g,i}c_{p,g,i}T) = \nabla(k_{eff}\nabla T) + S_{pc} + S_{\Omega}$	(7)
Ionic charge		
Carbon phase [39]	$\nabla(\sigma_c\nabla\phi_c) - R_{ox} + R_{red} = 0$	(8)
Membrane phase [39]	$\nabla(\sigma_m\nabla\phi_m) + R_{ox} - R_{red} = 0$	(9)

Table 3
Source terms used in the corresponding governing equations for a passive liquid-feed DMFC system described in Table 2.

Source term	Equation	
Liquid phase		
Total liquid reaction rate ($kg\,m^{-3}\,s^{-1}$)	$S_{\dot{m}_l} = \sum \dot{m}'''_{l,r,i} + \sum \dot{m}'''_{T,gl,i}$	(10)
Darcy pressure drop ($Pa\,m^{-1}$) [44]	$S_{l,dar} = -\frac{\mu_l}{k_{rl}k}\left(\varepsilon s \left\langle V_l \right\rangle^l\right)$	(11)
Electro osmotic drag ($Pa\,m^{-1}$)	$S_{l,ele} = \frac{\mu_l}{k_{rl}k\rho_l}\left(\frac{n_d(1-x_{MeOH})M_{H_2O} + (x_{MeOH})M_{MeOH}I}{F}\right)$	(12)
Liquid methanol reaction rate ($kg\,m^{-3}\,s^{-1}$)	$\dot{m}'''_{l,r,MeOH} = -\frac{R_{ox}M_{MeOH}}{6F}$	(13)
Liquid water reaction rate ($kg\,m^{-3}\,s^{-1}$)	$\dot{m}'''_{l,r,H_2O} = \left(-\frac{R_{ox}}{6F} + \frac{R_{red}}{2F}\right)M_{H_2O}$	(14)
Gas phase		
Total gas reaction rate ($kg\,m^{-3}\,s^{-1}$)	$S_{\dot{m}_g} = \sum \dot{m}'''_{g,r,i} - \sum \dot{m}'''_{T,gl,i}$	(15)
Darcy pressure drop ($Pa\,m^{-1}$) [44]	$S_{g,dar} = -\frac{\mu_g}{k_{rl}k}\left(\varepsilon(1-s)\left\langle V_g \right\rangle^g\right)$	(16)
Gas carbon dioxide reaction rate ($kg\,m^{-3}\,s^{-1}$)	$\dot{m}'''_{g,r,CO_2} = \frac{R_{ox}M_{CO_2}}{6F}$	(17)
Gas oxygen reaction rate ($kg\,m^{-3}\,s^{-1}$)	$\dot{m}'''_{g,r,O_2} = -\frac{R_{red}M_{O_2}}{4F}$	(18)
Thermal energy		
Heat source due to phase change ($W\,m^{-3}$) [39]	$S_{pc} = \sum \dot{m}'''_{T,gl,i}h_{fg,i}$	(19)
Heat source due to Ohmic heating ($W\,m^{-3}$) [39]	$S_\Omega = \nabla(\phi_m\sigma_m\nabla\phi_m) + \nabla(\phi_c\sigma_c\nabla\phi_c)$	(20)
Potential		
Oxidation reaction rate ($A\,m^{-3}$) [39]	$R_{ox} = a_{ox}I^{MeOH}_{0,ref}\frac{C_{MeOH}}{C_{MeOH} + \lambda\ \exp(\alpha_a\eta_a(F/R_uT))}\exp\left(\alpha_a\eta_a\frac{F}{R_uT}\right)$	(21)
Reduction reaction rate ($A\,m^{-3}$) [39]	$R_{red} = a_{red}I^{O_2}_{0,ref}\frac{\omega_{O_2}}{\omega_{O_2,ref}}\exp\left(-\alpha_c\eta_c\frac{F}{R_uT}\right)$	(22)

- The transient term in the electrochemical potential equation is neglected.
- Non-porous solid boundaries insulate the cell from the ambient.
- The effect of dissolved water on the water transportation through the membrane is neglected.
- Complete MeOH oxidation (no partial or side reactions) is assumed.
- For condensable gases, the vapor and liquid phases are in the thermal and chemical equilibrium condition.

The governing equations, including conservation of mass, species, momentum in the liquid and gas phases, ionic charge, energy and mass conservation for each species, are presented in Table 2. The source terms are given in Table 3. The constitutive relations describing the reaction rate, effective transport properties in the mixture, and kinetic properties are presented in Table 4. The physicochemical parameters used in the present numerical simulation are provided in Table 5. Table 6 presents the boundary conditions in the solution domain in the x-direction.

Table 4
Correlations in the corresponding governing equations in Table 2, for a passive liquid-feed DMFC system.

Parameter	Defining equation	
Capillary force [39]	$\left\{P_c = P_g - P_l = \sigma\cos\theta_c\left(\frac{\varepsilon}{k}\right)^{0.5}J(s),\quad J(s) = \begin{cases} 1.417(1-s) - 2.120(1-s)^2 + 1.263(1-s)^3 & \theta < \pi/2 \\ 1.417s - 2.120s^2 + 1.263s^3 & \theta \geq \pi/2 \end{cases}\right.$	(23)
Effective diffusivity [44]	$[D_{eff,ij}] = \mathbf{A}^{-1}\mathbf{B}$ $A_{ii} = -\frac{\omega_{g,i}M_g^2}{D_{iN}M_NM_i} - \sum_{\substack{k=1 \\ k\neq i}}^{N}\frac{\omega_{g,k}M_g^2}{D_{ik}M_kM_i};\quad A_{ij} = -\omega_{g,i}\frac{M_g^2}{M_i}\left(\frac{1}{D_{ij}M_j} - \frac{1}{D_{iN}M_N}\right);\quad i\neq j$ $B_{ii} = -\frac{M_g}{M_i}\left(1 - \frac{M_g\omega_{g,i}}{M_i}\right) - \frac{M_g^2\omega_{g,i}}{M_iM_N};\quad B_{ij} = \frac{M_g^2\omega_{g,i}}{M_iM_N}\left(\frac{1}{M_j} - \frac{1}{M_N}\right);\quad i\neq j$	(24)
Effective thermal conductivity [39]	$k_{eff} = \varepsilon s k_l + \varepsilon(1-s)k_g + (1-\varepsilon)k_s$	(25)
Equilibrium balance in liquid/gas interface [39]	$\omega_{g,i} = \omega_{l,i}\beta_i,\qquad \beta_i = \frac{M_lP_{ref}}{M_gP_v}\exp\left(\frac{h_{fg}M_i}{R}\left(\frac{1}{T_{ref}} - \frac{1}{T}\right)\right)$	(26)
Gas effective density	$\rho_g = \frac{P_g}{R_uT\sum(\omega_j/M_j)}$	(27)
Volume fraction of methanol in liquid phase	$\alpha_{l,MeOH} = \frac{\omega_{l,MeOH}\rho_{l,H_2O}}{(1-\omega_{l,MeOH})\rho_{l,MeOH} + \omega_{l,MeOH}\rho_{l,H_2O}}$	(28)
Volume weighted property in liquid phase	$\Phi_{l,eff} = \alpha_{l,MeOH}\Phi_{l,MeOH} + (1-\alpha_{l,MeOH})\Phi_{l,H_2O}$	(29)
Heat transfer coefficient on the air breathing inlet	$h = Nu\frac{k}{L};\quad Nu = 0.27(Gr\,Pr)^{0.25};\quad Gr = \frac{g\rho\lvert\Delta\rho\rvert L^3}{\mu^2}$	(30)
Mass transfer coefficient on the air breathing inlet	$h_{m1} = Sh\frac{\rho D_{ij}}{L};\quad Sh = 0.27(Gr\ Sc)^{0.25}$	(31)

Table 5
Geometry and physicochemical properties in the corresponding governing equations for a passive liquid-feed DMFC system.

Parameters	Value				
	Thickness, Porosity, Permeability, Tortuosity, Contact Angle				
	(m)	(ε)	(K, m^2)	(τ)	($\theta_{MeOH}/\theta_{H2O}$)
Hydrophobic porous medium (PW)	1e-2	0.8	2.5e-13	1.1	$0/\pi$
Hydrophilic porous medium (NPW)	9e-4	0.8	1.0e-10	1.1	0/0
Anode gas diffusion layer	1.5e-4	0.7	1.0e-11	1.0	0/0
Anode catalyst layer	2.3e-5	0.6	2.5e-12	1.8	0/0
Membrane	1.8e-4	0.5	1.0e-13	1.8	0/0
Cathode catalyst layer	2.3e-5	0.6	2.5e-12	1.8	0/0
Cathode gas diffusion layer	1.5e-4	0.7	1.0e-11	1.0	$0/(\pi/3)$
Air breathing layer	2.54e-4	0.2	7.24e-13	2.1	π/π

Diffusivity, Gas Phase, O_2/CO_2 $0.159\cdot10^{-4}$ [45] for proportionality of form $D_{ij} \propto p^{-1}T^{3/2}$

O_2/H_2O $0.244\cdot10^{-4}$

$O2/N_2$ $0.202\cdot10^{-4}$

CO_2/H_2O $0.162\cdot10^{-4}$

CO_2/N_2 $0.160\cdot10^{-4}$

H_2O/N_2 $0.242\cdot10^{-4}$

at 293K, 101.325kPa

$D_{ij} = D_{ji}$, (m^2/s),

O_2/MeOH, CO_2/MeOH, H_2O/MeOH, MeOH/N_2 Assumed $\left(\begin{array}{l}-0.06954+\\ 4.5986\cdot10^{-4}T+\\ 9.4979\cdot10^{-7}T^2\end{array}\right)\times10^{-4}$

Liquid Methanol Density [45] ($\rho_{\ell,MeOH}$, kg/m^3) $244.4\times0.224^{(-(1-T/573)^{2/7})}$

Liquid Diffusivity- [45] ($D_{H2O/MeOH}$, m^2/s) $10^{(-5.4163-999.778/T)}$

Liquid Water Density [44] (ρ_{ℓ,H_2O}, kg/m^3) $\exp\left(\begin{array}{l}6.9094-2.0146\times10^{-5}\ (T-273)\\ -5.968\times10^{-6}\ (T-273)^2+2.5921\times10^{-8}\ (T-273)^3\\ -9.3244\times10^{-11}\ (T-273)^4+1.2103\times10^{-13}\ (T-273)^5\end{array}\right)$

Viscosity of Gas Phase (μ_g, kg/ms) 1.0×10^{-5}

Viscosity of Liquid Water (μ_{ℓ,H_2O}, kg/ms) 1.03×10^{-3}

Viscosity of Liquid Methanol ($\mu_{\ell,MeOH}$, kg/ms) 5.39×10^{-4}

Electro-osmotic Drag Coefficient for Pure Water (n_d, mol/mol) 2.5

Electric Conductivity in Carbon Cloth (σ_c, Ω^{-1}m^{-1}) 4000

Electric Conductivity in Membrane (σ_m, Ω^{-1}m^{-1}) 3.4

Exchange Current Density in Anode [44] ($I^{MeOH}_{o,ref}$, A/m^2) $94.25\exp\ 35570/R_u(1/353-1/T)$

Exchange Current Density in Cathode [44] ($I^{O_2}_{o,ref}$, A/m^2) $0.0422\exp\ 73200/R_u(1/353-1/T)$

Specific Area in Anode (a_{ox}, m^{-1}) 35.65

Specific Area in Cathode (a_{red}, m^{-1}) 43478

Oxidation Constant (λ, mol/cm^3) 1.2×10^{-7}

Reduction Reference Mass Fraction ($\omega_{O_2,ref}$, kg/kg) 0.23

Thermodynamic Potential (U^{MeOH}, U^{O_2}, Volt) -0.029, 1.24

Eq. (1) describes the conservation of mass in the liquid phase; the source term reflects the mass generation rate due to the consumption or production rate via reaction at the catalyst layers and the condensation/evaporation rate of the liquid species. The momentum equation is expressed by the Navier–Stokes equation (Eq. (2)), which accounts for the fluid flow in the porous medium by Darcy's law (Eq. (11)) and the electro osmotic drag due to the ion conduction in the membrane (Eq. (12)). In this work, for the sake of simplicity, inertia and diffusive terms in Eq. (2) are neglected. The species equation for the liquid methanol is given by Eq. (3). The total mass rates include the reaction rate at the catalyst layers ($\dot{m}'''_{\mathrm{l,r},i}$) and the mass transfer rate of each species from gas phase to liquid phase ($\dot{m}'''_{\mathrm{T,gl},i}$). The governing equations ((4)–(6)) illustrate that the conservation of mass, momentum, and species in the gas phase have similar formulations to those in the liquid phase. By similar approximation, inertia and diffusive terms in Eq. (5) are neglected.

The thermal energy equation is expressed by Eq. (7) with the consideration of heat effect by ohmic heating (Eq. (20)) due to ionic resistance and internal energy change (Eq. (19)) due to the reaction at the electrodes. The electrochemistry in the anode and cathode is described by Eqs. (8) and (9). The oxidation and reduction rates are modeled from the expression developed by Mayers and Newman [19–21] and given by Eqs. (21) and (22). In Eq. (21), since λ is very small, the oxidation rate at the catalyst layer for large liquid methanol concentration is zero order and for low concentration is first order.

The diffusion of the gas in a multi-component mixture can be calculated from the Stefan–Maxwell relationship as described by

Table 6
Boundary conditions in the corresponding governing equations for a passive liquid-feed DMFC system in y-direction.

Governing Eqs.	$x=0$	$x=x_{agdl}$	$x=x_{acl}$	$x=x_{m}$	$x=x_{ccl}$	$x=x_{cgdl}$	$x=x_{ab}$	$x=x_{l}$
Momentum	$\nabla P_g \cdot n = 0$	N/A	N/A	N/A	N/A	N/A	N/A	$p_g = 0$
	$p_l = 0$	N/A	N/A	N/A	N/A	N/A	N/A	$\nabla p_l \cdot n = 0$
Gas transport	$\nabla \omega_{g,i} = 0$	N/A	N/A	N/A	N/A	N/A	N/A	$-[\varepsilon(1-s)]^{\tau}\rho_g D_{eff}\nabla\omega_{g,i}\cdot n = h_{m1}(\omega_{g,i}-\omega_{g,i,\infty})$
Liquid transport	$\omega_{l,i,res} = 1$	N/A	N/A	N/A	N/A	N/A	N/A	$\nabla\omega_{l,i}\cdot n = 0$
Membrane potential	N/A	N/A	$\nabla\phi_m\cdot n = 0$	N/A	N/A	$\nabla\phi_m\cdot n = 0$	N/A	N/A
Catalyst potential	N/A	$\phi_c = 0$	N/A	$\nabla\phi_c\cdot n = 0$	$\nabla\phi_c\cdot n = 0$	N/A	$\phi_c = V_{cell}$	N/A
Energy	$\frac{\partial T}{\partial x} = 0$	N/A	N/A	N/A	N/A	N/A	N/A	$-k_{eff}\nabla T\cdot n = h(T-T_\infty)$

Eq. (24). The liquid and gas phases are assumed to be in the thermal and chemical equilibrium and the liquid/gas mass fraction relation for the condensable gases is given by Raoult's law (Eq. (26)). Eq. (28) calculates the volume fraction of methanol in the liquid phase in each computational cell, which can be used to obtain all the liquid properties by using Eq. (29). In Eq. (29), Φ can be any liquid property.

It should be noted that the computational domain at $x = x_{ab}$ and $y_1 < y < y_2$, acts like a solid wall. Also, $y = 0$ is a symmetric line and all boundaries located at $y = y_2$, except the one that is in $x_{npw} < x < x_{agdl}$, are solid wall. The boundary conditions for $x_{npw} < x < x_{agdl}$ and $y = y_2$ are as follows:

$$p_l = 0, \quad p_g = 200, \quad \nabla\omega_{g,i} = 0, \quad \nabla\omega_{l,i} = 0, \quad \frac{\partial T}{\partial y} = 0$$

3. Numerical procedures

Governing equations given in Table 2 are discritized based on finite volume approach by using an up-wind scheme for convective terms [47]. Numerical procedure includes three steps. First of all, finding the relation between liquid pressure, gas pressure and liquid saturation; secondly, solving species equations; and thirdly, solving the energy equation. To capture the detail of the phenomena at the interfaces, a non-uniform grid in the x-direction is applied in which a total 80 cells in the x-direction and 12 cells in the y-direction are used. A polarization curve was made with this grid and compared to a grid with a doubled number of cells in both x- and y-directions. The cell current density was within 0.5% at each voltage.

3.1. Calculation of liquid saturation and pressures

Combination of Eqs. (1) and (2) is discretized in the following form:

$$a_{ls}s + a_{pl}p_l = b_l \tag{32}$$

In the same fashion for the combination of Eqs. (4) and (5), the following discretized equation can be written:

$$a_{gs}s + a_{pg}p_g = b_g \tag{33}$$

Since there are three unknowns in Eqs. (32) and (33), a saturation weighted pressure is defined as follows:

$$\bar{p} = sp_l + (1-s)p_g \tag{34}$$

Using the capillary pressure, p_l and p_g are written as a function of two variables; s and $\bar{p}$.

$$p_l = \bar{p} - (1-s)p_c, \qquad p_g = \bar{p} + sp_c \tag{35}$$

Since p_l and p_g in Eq. (35) are functions of liquid saturation, they cannot be directly plugged in Eqs. (32) and (33). Linearization of Eq. (35) follows as:

$$p_l^{k+1} = \bar{p}^{k+1} - [(1-s)p_c]^{k+1}, \quad [(1-s)p_c]^{k+1} = [(1-s)p_c]^k + \left(\frac{\partial((1-s)p_c)}{\partial s}\right)^k (s^{k+1}-s^k) \tag{36}$$

Performing the same procedure for gas pressure and plugging the result in Eqs. (32) and (33), the following equation is obtained to solve the liquid saturation:

$$\begin{aligned}\left(a_{ls} - a_{pl}\frac{\partial((1-s)p_c)^k}{\partial s}\right)s^{k+1} + a_{pl}\bar{p} &= b_l - a_{pl}\left(-(1-s)p_c + \frac{\partial((1-s)p_c)}{\partial s}s\right)^k \\ \left(a_{gs} + a_{pg}\frac{\partial(sp_c)^k}{\partial s}\right)s^{k+1} + a_{pg}\bar{p} &= b_g - a_{pg}\left(sp_c - \frac{\partial(sp_c)}{\partial s}s\right)^k\end{aligned} \tag{37}$$

3.2. Calculation of liquid and vapor methanol mass fractions

Since the condensation rate ($\dot{m}'''_{T,gl,i}$) is considered as a flow variable, the gaseous methanol and water mass fractions are given as a function of the methanol mass fraction in the liquid phase (Eq. (26)). The governing equation for the methanol mass fraction in the gas phase can be rewritten as:

$$\frac{D}{Dt}(\varepsilon(1-s)\rho_g\beta_{MeOH}\omega_{l,MeOH}) = \nabla\cdot\left([\varepsilon(1-s)]^{\tau}\rho_g D_{eff,ij}\beta_{MeOH}\nabla\omega_{l,MeOH}\right) + \dot{m}'''_{g,r,MeOH} - \dot{m}'''_{T,gl,MeOH} \tag{38}$$

In the same fashion, the governing equation for the liquid methanol mass fraction is:

$$\frac{D}{Dt}(\varepsilon s\rho_l\omega_{l,MeOH}) = \nabla\cdot([\varepsilon s]^{\tau}\rho_l D_{l,12}\nabla\omega_{l,MeOH}) + \dot{m}'''_{\ell,r,MeOH} + \dot{m}'''_{T,g\ell,MeOH} \tag{39}$$

Combining Eqs. (38) and (39), the condensation rate can be eliminated and the mass fraction of liquid methanol is determined. Then, the mass fraction of gaseous methanol is calculated by using Eq. (26). Now, the condensation rate of the methanol is obtained by using Eq. (39):

$$\dot{m}'''_{T,gl,MeOH} = b_l - a_l\omega_{l,MeOH} \tag{40}$$

where b_l and a_l are the coefficient in the discretized equation.

Since the liquid water mass fraction is determined by the balance of mass fractions, the mass fraction of water cannot be determined by the same procedure as methanol. In order to prevent the evaporation rate of water from being extremely large, a check has to be performed by comparing the calculated value with the maximum liquid water that can actually be evaporated. Maximum evaporated liquid water is:

$$(\dot{m}'''_{gl,H_2O})_{max} = -\left(\frac{(\varepsilon s\rho_l\omega_{l,H_2O})^n}{\Delta t} + \int\nabla\dot{m}_{l,H_2O}\,dV + \dot{m}'''_{r,l,H_2O}\right) \tag{41}$$

where $(\varepsilon s \rho_l \omega_{l,H_2O})^n / \Delta t$ is the total existing liquid water per volume of computational cell in the previous time step.

3.3. Numerical solution procedure

The numerical steps for the calculation are as follows:

1. Setting the initial conditions of temperature, velocity, potentials, mass fractions and pore properties in each layer of the fuel cell.
2. Updating all the non-linear properties and coefficients.
3. Solving the electric potential in the membrane and the carbon cloth and updating electrochemical reaction source terms (Eqs. (8) and (9)).
4. Solving for liquid saturation, liquid pressure, and gas pressure using Eqs. (1), (2), (4), (5), and (23).
5. Calculating liquid and gas velocities.
6. Solving for the gaseous and liquid mass fractions (Eqs. (3) and (6)).
7. Solving the energy equation (Eq. (7)).
8. Going to step 2 and repeating the loop until a converged result is obtained.

4. Results and discussions

The results are presented in five sections. First, the numerical model and all constants involved in the model are validated through the polarization curve compared to the experimental result. Secondly, fuel cell performance is investigated. In the third part, the transient behavior of the system is studied. The last two sections are devoted to steady state characteristic and investigation on the semi passive system, respectively.

4.1. Validation of the model

Fig. 2 shows the polarization and power density curve when only five main layers of a DMFC are considered. For this case, a 3 M solution in a reservoir right above the anode gas diffusion layer is applied, while the cathode side is exposed to air at 300 K. The numerical simulation results are compared to the experimental results of Guo and Faghri [8] and show a good agreement. A comparison has also been made between an isothermal and a non-isothermal model. As shown in this figure, since an isothermal model cannot capture the temperature increase in the cell, it predicts lower power density than a non-isothermal model. All constants in governing equations are calibrated according to this result.

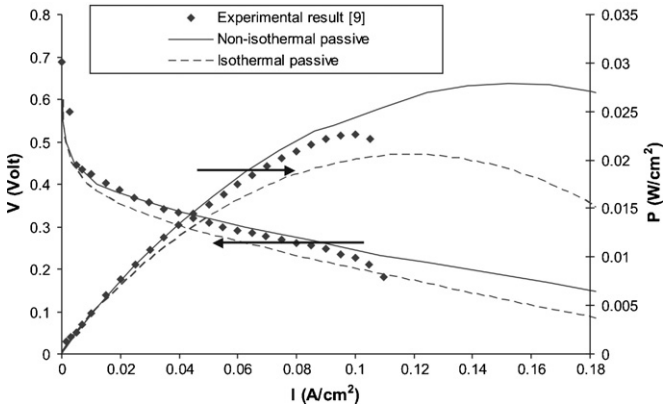

Fig. 2. Polarization and power density curve when a 3 M solution is applied directly to the anode gas diffusion layer at ambient temperature of 300 K.

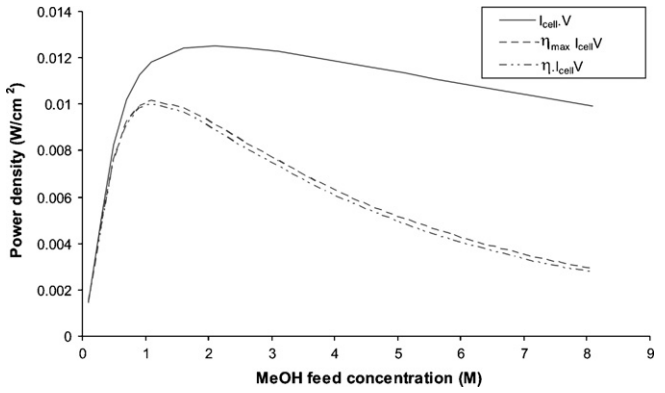

Fig. 3. Power density versus methanol feed concentration under constant cell voltage of 0.25 V.

4.2. Fuel cell performance

During fuel cell operation, methanol is wasted or consumed by evaporation loss, crossover loss and the useful current in the anode. In order to investigate the fuel utilization, the concept of fuel consumption efficiency is introduced to measure the ratio of fuel used to create power to the total consumed fuel. The fuel consumption efficiency (η) and the maximum fuel consumption efficiency (η_{max}), assuming full recovery of the evaporated methanol, are defined as follows:

$$\eta = \frac{I_{cell}}{I_{cell} + I_{crossover} - (6F/M_{MeOH}A)\int \dot{m}'''_{T,gl,MeOH}\, dV},$$

$$\eta_{max} = \frac{I_{cell}}{I_{cell} + I_{crossover}} \tag{42}$$

Fig. 3 shows the power density variations with and without considering fuel consumption efficiency versus different methanol feed concentrations at a reservoir right above the anode gas diffusion layer. The power density increases with the methanol feed concentration when it is less than 2 M. Considering fuel consumption efficiency (η), the maximum power density decreases and shifts to a lower feed concentration.

Fig. 4 shows the methanol consumption contributed by evaporation loss, crossover loss, and the useful current under different methanol feed concentrations at the reservoir right behind the anode gas diffusion layer for a constant voltage of 0.25 V. At the lower methanol concentration, the increasing rate of useful current is positive until the concentration reaches 2 M and then decreases

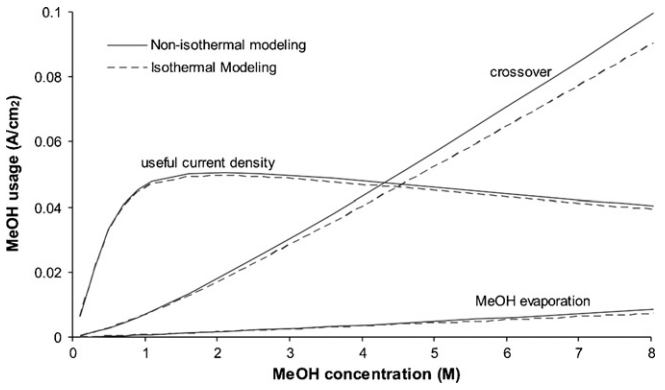

Fig. 4. A comparison between an isothermal and a non-isothermal prediction for three mechanisms of the methanol usage at constant cell voltage of 0.25 V.

because the crossover phenomenon becomes significant. At about 4.3 M feed concentration, the crossover loss is greater than the cell current. Since crossover loss is mainly due to methanol diffusion, it monotonically increases with the methanol concentration. Evaporation loss is one of the contributors to the fuel loss, which is increased with concentration feed at the reservoir. However, it is notable that compared to the result of an isothermal, non-equilibrium model [27], the non-isothermal model predicts much less evaporation loss which can be attributed to the empirical correlations used for non-equilibrium model.

The power output of the fuel cell is determined by the main operating conditions such as methanol feed concentration and the cell voltage. Fig. 5 displays the contour of cell power density with and without consideration of the fuel consumption efficiency (η) as a function of methanol feed concentration at a reservoir right above the anode gas diffusion layer, and as a function of the cell voltage. Without considering fuel consumption efficiency (Fig. 5a), the maximum power density of the fuel cell is 35 mW cm^{-2}. The corresponding feed concentration is between 0.24 and 5.5 M and the corresponding cell voltage is between 0.18 and 0.24 V. If the crossover loss and evaporation loss are considered in the power density, the maximum power density of the fuel cell decreases to a value of 14 mW cm^{-2}. The corresponding feed concentration and cell voltage are between 2 and 3.2 M and between 0.19 and 0.21 V, respectively. The recovery of methanol evaporation can be very effective in real applications.

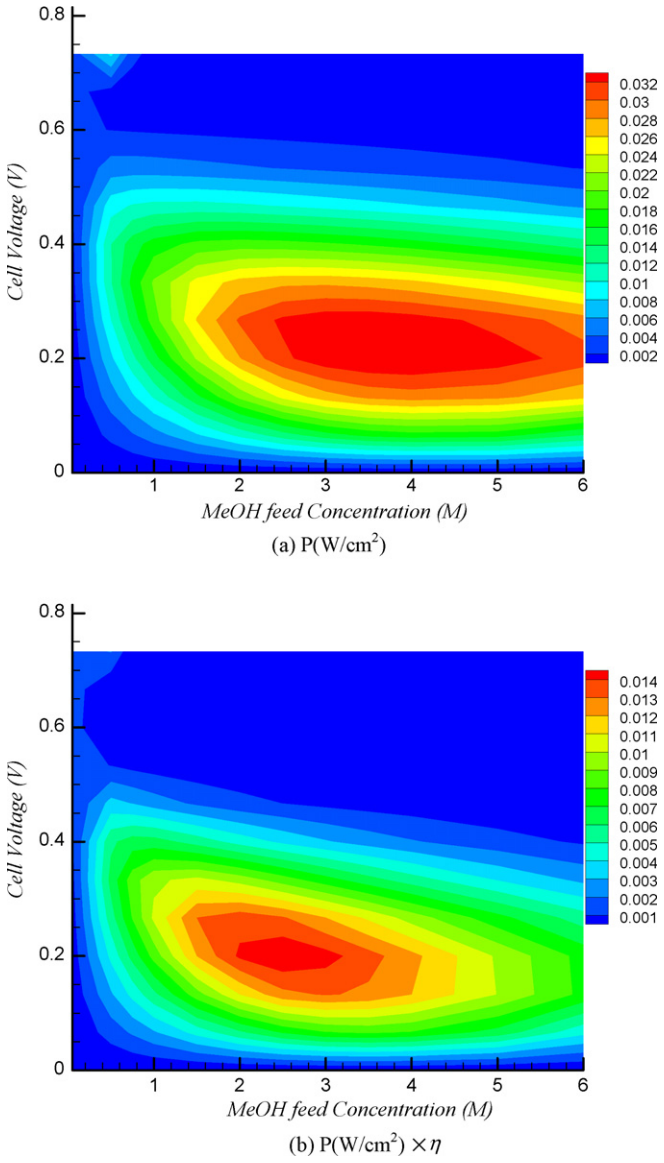

Fig. 5. Contour plots of cell power density (a) without and (b) with consideration of fuel consumption efficiency as a function of MeOH feed concentration and the cell voltage.

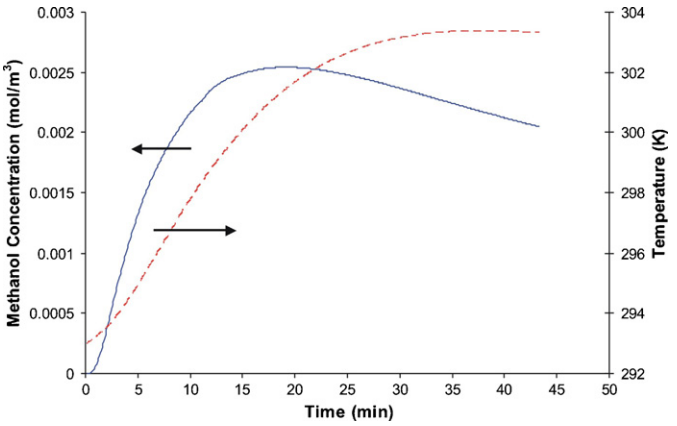

Fig. 6. Variations of methanol concentration at the anode gas diffusion layer and the temperature at the air breathing layer versus time under the constant voltage of 0.35 V and feed concentration of the pure methanol (24 M) in the reservoir.

4.3. Transient characteristics

Considering whole porous layers shown in Fig. 1, Fig. 6 depicts the variation of temperature at the end of an air breathing layer ($x = x_l$) and the methanol concentration at the anode gas diffusion layer with time. The temperature has a sharp increase rate during the first 15 min, and after that it starts to decrease. The temperature reaches a steady value after almost 85 min. The temperature raises as much as 10 °C. Variation of methanol concentration versus time at the anode porous layers is important. As shown in this figure, liquid methanol concentration at the anode gas diffusion layer increases initially for 19 min. After that, it starts to decrease to a steady value of 2 M.

Fig. 7 shows the three types of fuel consumption variation versus time in the fuel cell. The evaporation loss contributes one of the main portions of fuel consumption, even though it is smaller than the other two. At the beginning, crossover fuel consumption increases more slowly than the useful current while the evaporation loss is small. After about 23 min, the crossover begins to decrease. The crossover loss becomes greater than the cell current after 6 min and becomes smaller than the cell current again

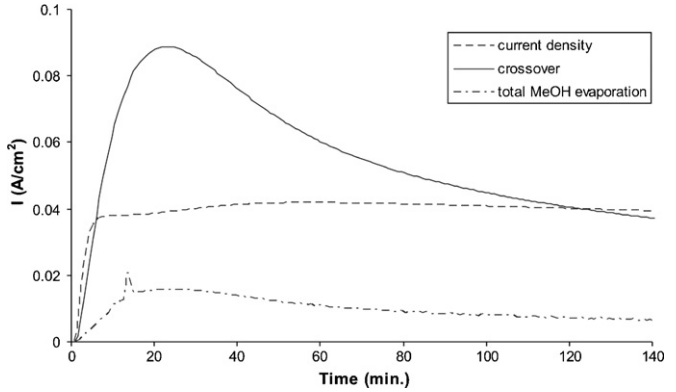

Fig. 7. Variations of methanol usage with time under the constant voltage of 0.35 V and feed concentration of the pure methanol (24 M) at the reservoir.

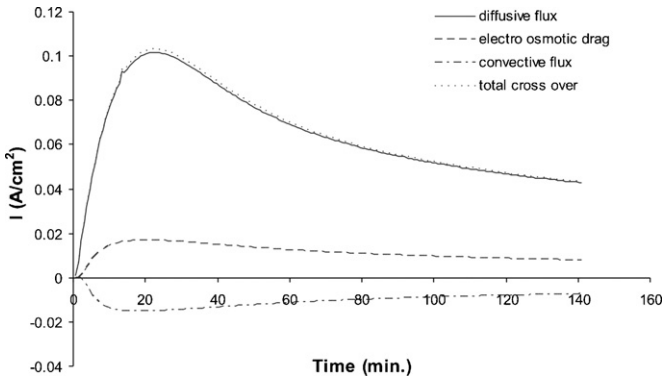

Fig. 8. Variations of three mechanisms of the methanol crossover versus time under the constant voltage of 0.35 V and feed concentration of the pure methanol (24 M) at the reservoir.

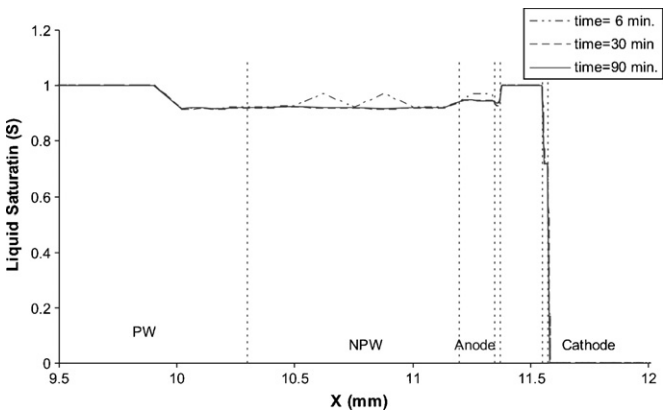

Fig. 10. Area averaged liquid saturation distribution in the fuel delivery system and fuel cell at different times for a cell voltage of 0.35 V.

after about 120 min. While the crossover needs a longer time to reach a steady value, useful current density reaches its steady state situation much faster. The evaporation loss increases relatively slowly and after about 20 min, reaches the highest value and starts to decrease. Finally it reaches a steady value after almost 120 min.

Fig. 8 shows the three mechanisms of methanol crossover variation through the membrane versus time. All values are calculated at the first cell of the membrane in the anode side. The contributions of diffusion, electro osmotic drag and convection are illustrated. The diffusion and electro osmotic drag initially increase due to the increase in the feed concentration at the inlet of the MEA. The negative capillary pressure increases to push some of the liquid methanol back to the anode side. The increasing rate of diffusion stops after about 22 min due to the decreasing concentration gradient at the anode (as shown in Fig. 6). The electro osmotic drag begins to decrease after 22 min because of the same reason. Electro osmotic drag of the liquid methanol through the membrane is directly related to the methanol molar fraction. This figure also shows the total methanol crossover due to all three mechanisms. This summation is relatively higher than the crossover shown in Fig. 7. This is due to evaporation of some of the liquid methanol migrated to the cathode side and has not participated in the electrochemical reduction reaction.

Distribution of the liquid methanol concentration through all porous layers, shown in Fig. 1, is important to have a proper methanol concentration at the anode catalyst layer and reduce the crossover. In order to reveal the methanol transport through the fuel delivery and fuel cell, methanol concentration at the different times are presented in Fig. 9. In this figure, 'PW' refers to the preferential porous medium (wick) and 'NPW' stands for the non-preferential porous medium (wick). The driving force in the methanol transport is mainly diffusion and advection by the capillary pressure. As demonstrated in Fig. 6, Fig. 9 shows that the methanol concentration at the anode gas diffusion layer initially increases and, after reaching a pick point, finally decreases until reaching to a steady value. Liquid methanol migrated to the cathode catalyst layer either is evaporated or takes part in the oxidation reaction.

Fig. 10 depicts the liquid saturation distribution in the fuel delivery system and fuel cell at different times when pure methanol is fed by the fuel reservoir for a cell voltage of 0.35 V. The liquid saturation becomes unity at the membrane where electro osmotic force draws the liquid water and methanol through the membrane. Since hydrophobic materials are used in the cathode and air breathing layer to push the liquid water into the anode and preventing the liquid drop formation, the saturation in the cathode and air breathing layer nearly reaches zero. So the diffusive resistance for O_2 is very small, and there is a very small drop in the O_2 mass fraction at the cathode side.

Fig. 11 illustrates the temperature distribution in the fuel delivery system and the fuel cell over time for pure methanol at the reservoir and the cell voltage of 0.35 V. As shown already in Fig. 6, the air breathing layer temperature increases monotonically over time until reaching a steady value. Fig. 11 depicts this trend as well. Due to the electrochemical reaction and presence of the natural convection at the cathode air breathing layer, the system temperature increases as much as 10 °C relative to the reference temperature. The distribution of temperature through all the layers is nearly uniform for all times, with a very small increase at the

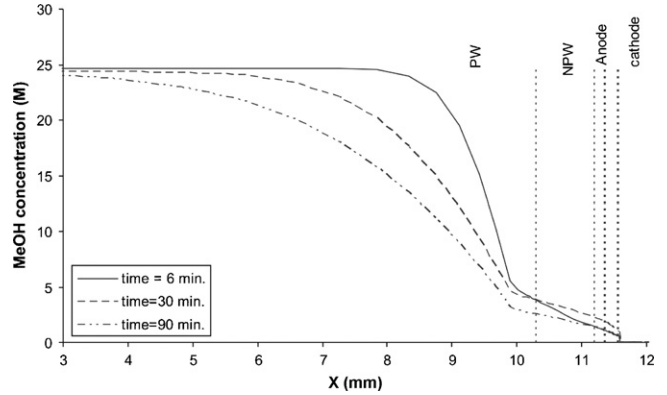

Fig. 9. Area averaged methanol concentration through the fuel delivery system and fuel cell at different times for a cell voltage of 0.35 V.

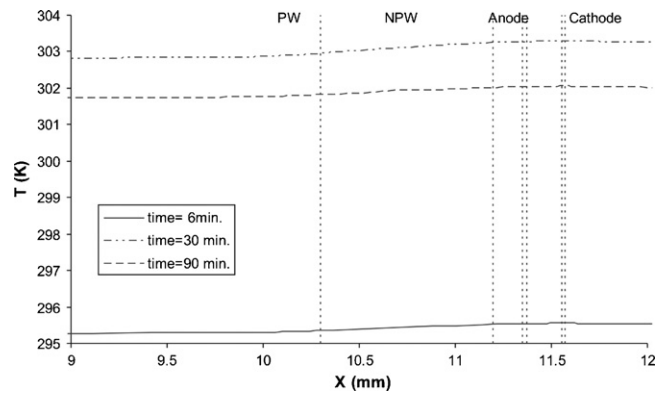

Fig. 11. Area averaged temperature distribution in the fuel delivery system and fuel cell at different times for a cell voltage of 0.35 V.

five main layers of the DMFC mainly due to the electrochemical reaction at the electrodes.

4.4. Steady state operation

To get the steady state results, special care should be taken to make sure that all variables involved in the problem reach their steady state situation. Looking at Figs. 6–8, one concludes that each variable needs a different number of time steps to reach the steady state. The criterion for the steadiness of the total system is the variable that needs the greatest number of time steps. For instance, Fig. 12 demonstrates that even though liquid saturation (s) easily reaches the steady sate situation (after almost 20,000 time steps), CO_2 mass fraction needs many more time steps to reach its own steady state (more than 100,000 time steps). In this study, the steadiness of ω_{CO_2} is selected as a criterion for the whole system.

4.5. Effect of semi passive oxidant feeding on the DMFC performance

There are three effects associated with an active cathode in DMFC that can be considered. First of all, using convective heat transfer instead of natural convection decreases the temperature of the system. This effect is not favorable and deteriorates the performance. Secondly, from a mass transport point of view, it should facilitate the oxygen transfer to the cathode catalyst layer. If there is a limiting current density caused by lack of oxidant in the cathode, semi passive DMFC can be promising in this regard. Thirdly, using active mass transport enhances the moisture removal from the cathode gas diffusion layer and, in turn, reduces the resistance against oxidant diffusion toward the cathode catalyst layer. However, it is notable that existence of liquid droplets at the cathode catalyst layer can reduce the effective reduction reaction area. In a real semi passive system, due to using channel to direct the air to the cathode gas diffusion layer, the active heat and mass transfer area would be less than the one in the passive system which uses the whole cathode surface for natural heat and mass transfer. For the sake of simplicity, the fully developed heat transfer coefficient for a rectangular duct in which only one of longer edges (a) is responsible for heat and mass transfer and all three other edges are to be insulated, is used [46]. For an aspect ratio of 0.1 the mass transfer coefficient would be as follows:

$$Nu = 4.558$$
$$Nu = Sh(Le)^{-1/3} \quad \& \quad Le = \frac{\alpha}{D_{\mathrm{air},i}} \qquad (43)$$
$$h_{\mathrm{ml}} = \frac{Nu(Le)^{1/3}\rho D_{\mathrm{air},i}}{L}$$

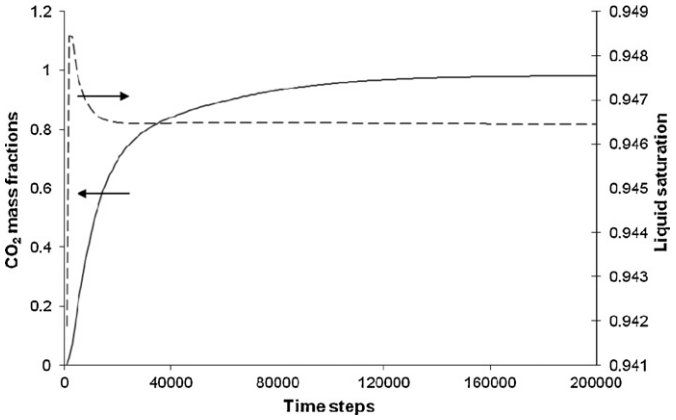

Fig. 12. Comparison between the number of time steps needed to get the steady state for liquid saturation (s) and CO_2 mass fraction (ω_{CO_2}).

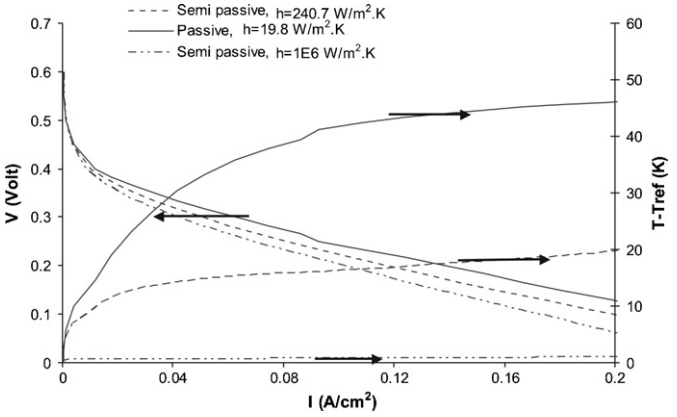

Fig. 13. Polarization curve and relative temperature of the air breathing layer for three different heat transfer coefficients when the reference ambient temperature is 300 K and the oxidant is transferred via natural convection.

The total length of the DMFC in the y-direction in the computational domain is used as the characteristic length. To see the effect of temperature, three cases are investigated; natural convection, forced convection described by Eq. (43), and infinite heat transfer coefficient. For all cases, the mass transport mechanism at the cathode is assumed to be natural convection mass transport. Fig. 13 shows the polarization curve and the temperature rise of an air breathing layer for three aforementioned conditions when the reference ambient temperature is 300 K. The heat transfer coefficient in this figure increases from 19.8 to 240.7 $W\,m^{-2}\,K^{-1}$, and finally to an infinite value. As seen in this figure, the cell performance decreases by increasing the heat transfer coefficient.

Increasing the mass transfer coefficient at the cathode is the other purpose of using a semi passive system. To see the pure effect of forced mass transfer at the cathode, it is assumed that the whole cell is kept at the same temperature as the reference temperature for all current densities. Fig. 14 shows the effect of increasing the mass transfer coefficient on the performance of an isothermal cell. In this figure, the mass transfer coefficient increases from $3.77 \times 10^{-3}\,kg\,m^{-2}\,s^{-1}$ for natural mass transfer to $0.3\,kg\,m^{-2}\,s^{-1}$ for forced mass transfer and finally to an infinite mass transfer coefficient. Fig. 15 depicts the oxygen mass fraction at the cathode side for two finite aforementioned mass transfer coefficients. It has been seen that there is no change in the oxygen mass fraction for the increase in the forced mass transfer coefficient from $0.3\,kg\,m^{-2}\,s^{-1}$ to the infinite.

Since the liquid saturation at the cathode due to using hydrophobic cathode gas diffusion and air breathing layers tends to be zero,

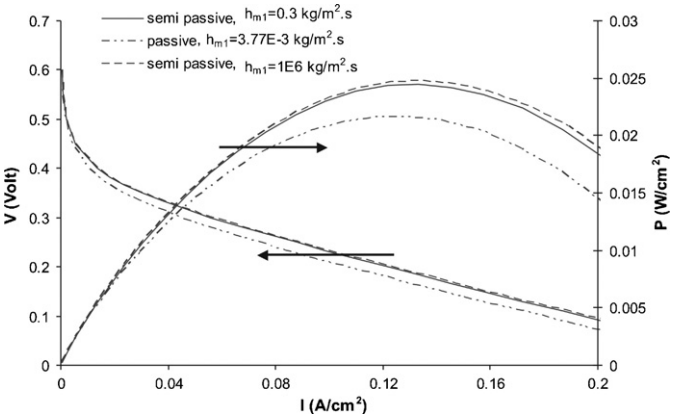

Fig. 14. Polarization curve and power density for three different mass transfer coefficients for an isothermal cell when the ambient temperature is 300 K.

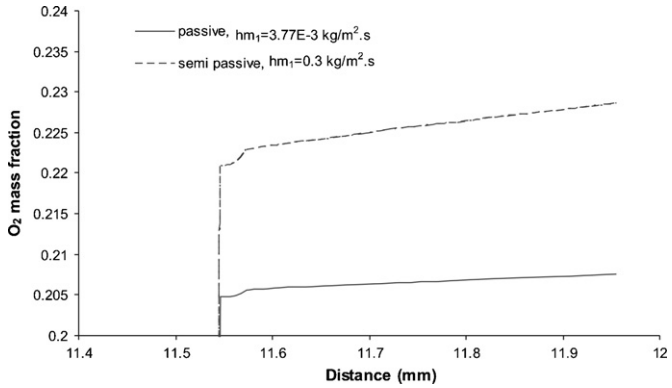

Fig. 15. Oxygen mass fraction at the cathode side for three different mass transfer coefficients for an isothermal cell when the ambient temperature is 300 K.

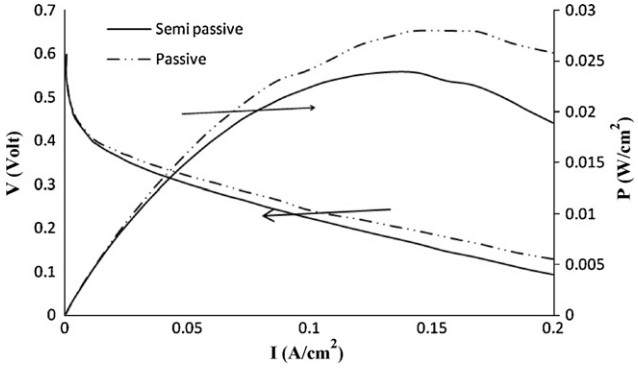

Fig. 16. Polarization and power density for the passive and semi passive system when the ambient temperature is 300 K.

study of the effect of liquid removal by using a semi passive system is not possible. Fig. 16 depicts the polarization curve and power density for passive and semi passive systems considering the effects of both the temperature and mass transfer. Even though better mass transfer improves the performance, the reduction of cell temperature due to the use of convection heat transfer is significant and reduces the power density, especially at the higher current densities where the temperature decrease is higher. In this figure, the heat and mass transfer coefficients for the cathode air breathing layers are 240.7 $W m^{-2} K^{-1}$ and 0.3 $kg m^{-2} s^{-1}$, respectively.

5. Conclusions

A two-dimensional, transient, multi-phase, multi-component model has been developed for a passive and semi passive liquid-feed DMFC including the fuel cell and the fuel delivery. The following conclusions can be drawn from this study:

- The cell temperature can increase during the operation and this leads to a higher current density, methanol crossover, and total methanol evaporation in comparison to an isothermal cell.
- A non-isothermal, chemical equilibrium model predicts much less total methanol evaporation in comparison to the one anticipated by an isothermal, non-equilibrium model. However, it is found that it is because of using the non-equilibrium model which, in turn, is due to a higher empirical interfacial transfer rate constant.
- Even though the cell temperature increases during the operation, the temperature distribution is almost uniform through all porous layers including the fuel delivery system and fuel cell.
- For a semi passive DMFC, different effective parameters have been investigated independently. It is found that during the operation of the cell, at a cell voltage of 0.35 V, the temperature of a completely passive cell is 15 °C higher than that in a semi passive cell, which, in sequence, results in a lower performance in the semi passive one. The temperature difference between these two systems increases at higher current densities. However, the mass transport of oxidant in a semi passive cell is improved.
- A comparison between passive and semi passive cells shows that a passive cell has a better performance than a semi passive one as long as there is no cathode.

References

[1] A.S. Arico, S. Srinivasan, V. Antonucci, Fuel Cells 12 (2001) 133–161.
[2] M. Broussely, G. Archdale, J. Power Sources 136 (2004) 386–394.
[3] J.H. Wee, J. Power Sources 173 (2007) 424–436.
[4] S. Eccarius, B.L. Garcia, C. Hebling, J.W. Weidner, J. Power Sources 179 (2008) 723–733.
[5] F. Liu, C.Y. Wang, J. Electrochem. Soc. 154 (6) (2007) B514–B522.
[6] G.B. Jung, A. Su, C.H. Tu, Y.T. Lin, F.B. Weng, S.H. Chan, J. Power Sources 171 (2007) 212–217.
[7] C. Xu, Y.L. He, T.S. Zhao, R. Chen, Q. Ye, J. Electrochem. Soc. 153 (7) (2006) A1358–A1364.
[8] Z. Guo, A. Faghri, J. Power Sources 160 (2006) 1142–1155.
[9] Z. Guo, A. Faghri, J. Power Sources 160 (2006) 1183–1194.
[10] Z. Guo, A. Faghri, J. Power Sources 167 (2007) 378–390.
[11] H. Kim, J. Power Sources 162 (2006) 1232–1235.
[12] A. Faghri, Z. Guo, Int. J. Heat Mass Transf. 48 (2005) 3891–3920.
[13] D. Chu, R. Jiang, Electrochim. Acta 51 (2006) 5829–5835.
[14] B. Bae, B.K. Kho, T.H. Lim, I.H. Oh, S.A. Hong, H.Y. Ha, J. Power Sources 158 (2006) 1256–1261.
[15] J.J. Martin, W. Qian, H. Wang, V. Neburchilov, J. Zhang, D.P. Wilkinson, Z. Chong, J. Power Sources 164 (2007) 287–292.
[16] Y. Yang, Y.C. Liang, J. Power Sources 165 (2007) 185–195.
[17] Q.Z. Lai, G.P. Yin, J. Zhang, Z.B. Wang, K.D. Cai, P. Liu, J. Power Sources 175 (2008) 458–463.
[18] A.A. Kulikovsky, J. Appl. Electrochem. 30 (2000) 1005–1014.
[19] J.P. Meyers, J. Newman, J. Electrochem. Soc. 149 (6) (2002) A710–A717.
[20] J.P. Meyers, J. Newman, J. Electrochem. Soc. 149 (6) (2002) A718–A728.
[21] J.P. Meyers, J. Newman, J. Electrochem. Soc. 149 (6) (2002) A729–A735.
[22] J. Divisek, J. Fuhrmann, K. Gartner, R. Jung, J. Electrochem. Soc. 150 (6) (2003) A811–A825.
[23] Z.H. Wang, C.Y. Wang, J. Electrochem. Soc. 150 (4) (2003) A508–A519.
[24] E. Birgersson, J. Nordlund, M. Vynnycky, C. Picard, J. Electrochem. Soc. 151 (12) (2004) A2157–A2172.
[25] J. Ge, H. Liu, J. Power Sources 160 (2006) 413–421.
[26] J. Ge, H. Liu, J. Power Sources 163 (2006) 907–915.
[27] J. Rice, A. Faghri, Int. J. Heat Mass Transf. 49 (2006) 4804–4820.
[28] W Liu, C.Y. Wang, J. Power Sources 164 (2007) 189–195.
[29] V. Saarinen, O. Himanen, T. Kallio, G. Sundholm, K. Kontturi, J. Power Sources 172 (2007) 805–815.
[30] W.W. Yang, T.S. Zhao, J. Power Sources 174 (2007) 136–147.
[31] W Liu, C.Y. Wang, J. Electrochem. Soc. 154 (3) (2007) B352–B361.
[32] W.W. Yang, T.S. Zhao, C. Xu, Electrochim. Acta 53 (2007) 853–862.
[33] W.W. Yang, T.S. Zhao, Electrochim. Acta 52 (2007) 6125–6140.
[34] C. Xu, T.S. Zhao, W.W. Yang, J. Power Sources 178 (2008) 291–308.
[35] R. Chen, T.S. Zhao, W.W. Yang, C. Xu, J. Power Sources 175 (2008) 276–287.
[36] T.Z. Yan, T.Ch. Jen, Int. J. Heat Mass Transf. 51 (2007) 1192–1204.
[37] B. Xio, A. Faghri, Int. J. Heat Mass Transf. 51 (2008) (2008) 3127–3143.
[38] J. Rice, A. Faghri, Int. J. Heat Mass Transf. 51 (2008) 948–959.
[39] J. Rice, A. Faghri, Thermal and start-up characteristics of a miniature passive liquid feed DMFC system, including continuous/discontinuous phase limitations, J. Heat Transf. 130 (6) (2008) 062001.
[40] W.W. Yang, T.S. Zhao, J. Power Sources 185 (2008) 1131–1140.
[41] B. Xiao, A. Faghri, Int. J. Heat Mass Transf. 52 (2009) 3525–3533.
[42] G. Jewett, A. Faghri, B. Xiao, Int. J. Heat Mass Transf. 52 (2009) 3564–3575.
[43] B.L. García, V.A. Sethuraman, J.W. Weidner, R.E. White, J. Fuel Cell Sci. Technol. 1 (2004) 43–48.
[44] A. Faghri, Y. Zhang, Transport Phenomena in Multiphase Systems, Elsevier Inc., 2006.
[45] C.L. Yaws, Handbook of Transport Property Data: Viscosity, Thermal Conductivity and Diffusion Coefficients of Liquids and Gases, Gulf Pub. Co., Houston, TX, 1995.
[46] M. Spiga, G.L. Morini, Int. J. Heat Mass Transf. 39 (1996) 1165–1174.
[47] S.V. Patankar, Numerical Heat Transfer and Fluid Flow, Hemisphere Publishing Corporation, 1980.